

# Enhancing Charge Transfer in Perovskite-Inspired Silver Iodobismuthate-Based Solar Cells via Cesium Iodide Interlayer

Basheer Al-Anesi, Vipinraj Sugathan, Joshua K. G. Karlsson, Amit Tewari, Roshan Nasare, Paavo Mäkinen, Debjit Manna, Matti Mäntysalo, and Paola Vivo\*

**Ag<sub>3</sub>BiI<sub>6</sub> (ABI) is one of the most widely explored lead-free perovskite-inspired materials for eco-friendly solar cell applications. However, despite the intense research efforts, the photovoltaic performance of ABI-based devices remains very modest, primarily due to poor film morphology and ineffective charge extraction. This work aims at investigating the potential benefits of a thermally evaporated cesium iodide (CsI) interlayer on the performance of ABI-based solar cells. Upon the addition of CsI atop the ABI layer in the device stack, the solar cells deliver a power conversion efficiency (PCE) of 2.27%. This is the highest efficiency reported for ABI solar cells employing a similar device architecture. It is found that the enhancement in PCE is largely due to improvement in the ABI|hole transport layer interface upon the introduction of CsI interlayer. The improvement is largely ascribed to enhanced surface coverage upon introduction of CsI interlayer, as evidenced by our comprehensive microscopy studies. Furthermore, impedance spectroscopy analysis is employed to provide further insights into the changes in charge transfer dynamics interlayer that dictate the enhancement of fill factor and short-circuit current density in the devices. The findings indicate that the addition of CsI promotes charge transfer and minimizes recombination losses.**

## 1. Introduction

Lead halide perovskites (LHPs) are at the forefront among the next-generation semiconductors for photovoltaic technologies, primarily because of their defect tolerance and outstanding optoelectronic properties that have led to the development of cost-effective devices with remarkable PCE, already surpassing 26%.<sup>[1,2]</sup> However, the commercial acceptance of LHP-based solar cells is still questionable due to instability and environmental toxicity concerns due to the presence of lead II cation (Pb<sup>2+</sup>) that might leach into the surrounding environment upon device decomposition.<sup>[3–6]</sup> Exploring less toxic perovskite-inspired materials (PIMs) is a promising approach to identify safer alternatives to LHPs.<sup>[7]</sup> In particular, pnictogen-based halides comprising Group VA cations *viz.* Bi (III) and Sb(III) are interesting because of their low toxicity and typically high light absorption coefficients. Moreover, pnictogen-based halides contain cations with intrinsically

stable oxidation states, which allow overcoming another typical drawback of LHPs and Sn<sup>2+</sup>/Ge<sup>2+</sup>-based PIMs, *i.e.*, their modest stability toward, for example, oxygen, moisture, and high temperature. Among the plethora of possible pnictogen-based halide PIMs, silver (Ag) iodobismuthates are among the most explored ones due to their high absorption coefficients, direct optical bandgaps (1.7–1.9 eV), low toxicity, and high air-stability.<sup>[8–10]</sup>


Typically, silver iodobismuthates are represented by the formula Ag<sub>x</sub>Bi<sub>y</sub>I<sub>(x+3y)</sub> and can stabilize in several stoichiometries.<sup>[11,12]</sup> They can be categorized into two groups based on silver content, “Ag-poor” compounds, including AgBiI<sub>4</sub>, AgBi<sub>2</sub>I<sub>7</sub>, and AgBi<sub>3</sub>I<sub>10</sub>, or “Ag-rich” compounds such as Ag<sub>3</sub>BiI<sub>6</sub> and Ag<sub>2</sub>BiI<sub>5</sub>. These distinctions in Ag content influence the arrangement of atoms in the crystal lattice.<sup>[10]</sup>

ABI is one of the most studied compositions among the silver bismuth iodide variants, with a bandgap of 1.79–1.83 eV.<sup>[9,13,14]</sup> ABI exhibits a rhombohedral phase characterized by the R-3 m space group consisting of edge-sharing (Ag/Bi)I<sub>6</sub> octahedra and extra Ag<sup>+</sup> cations filling the voids between the layers. Among pnictogen-based halides, ABI stands out as the most promising material with reported PCE (4–5%)<sup>[14,15]</sup> using

B. Al-Anesi, V. Sugathan, J. K. G. Karlsson, P. Mäkinen, D. Manna, P. Vivo Hybrid Solar Cells, Faculty of Engineering and Natural Sciences Tampere University  
P.O. Box 541, Tampere FI-33014, Finland  
E-mail: paola.vivo@tuni.fi

A. Tewari, M. Mäntysalo  
Faculty of Information Technology and Communication Sciences  
Tampere University  
Tampere 33720, Finland

R. Nasare  
Smart Photonic Materials, Faculty of Engineering and Natural Sciences  
Tampere University  
P.O. Box 541, Tampere FI-33014, Finland

 The ORCID identification number(s) for the author(s) of this article can be found under <https://doi.org/10.1002/aesr.202400119>.

© 2024 The Author(s). Advanced Energy and Sustainability Research published by Wiley-VCH GmbH. This is an open access article under the terms of the Creative Commons Attribution License, which permits use, distribution and reproduction in any medium, provided the original work is properly cited.

DOI: 10.1002/aesr.202400119

poly(bis(4-phenyl)(2,4,6-trimethylphenyl)amine (PTAA)) as hole transport layer (HTL). While numerous attempts have been made to further improve the photovoltaic performance of ABI-based cells, most of them focused on the fine-tuning of the light absorber, ABI, itself. For example, doping and alloying methods, viz. the incorporation of CuBr,<sup>[16]</sup> Na<sup>+</sup>, and Cs<sup>+</sup> ions,<sup>[17]</sup> have shown promise. Furthermore, the optimization of ABI synthesis, for example, by dynamic hot casting technique along with a ramped annealing,<sup>[18]</sup> and compositional engineering methods<sup>[19]</sup> have also been explored extensively. All these approaches have improved the PCE of corresponding ABI solar cells around 2%, as seen in most of the recent research.<sup>[16–19]</sup> However, ABI solar cells still suffer from significant hysteresis under illumination due to ion migration.<sup>[20]</sup> Indeed, the development of ABI-based solar cells and the understanding of their device physics is still at an early stage and only after careful engineering of the various device constituents, not limited to the light absorber, it will be possible to further improve the PCE while, at the same time, minimizing the hysteresis. For example, the influence of the LHP|HTL interface on the recombination dynamics of the charge carriers has been extensively explained in recent reports.<sup>[21,22]</sup> The careful engineering of this interface can lead to a reduced charge transfer resistance, which is desirable for efficient carrier conduction and low recombination losses at the interface.<sup>[21]</sup> One successful strategy for interface engineering is the introduction of passivation layers at the interface between the absorber and the HTL.<sup>[23]</sup> Conventionally, a range of materials have been employed for this in LHP-based solar cells. The materials that have been explored include organic polymers,<sup>[24]</sup> nanoparticles,<sup>[25]</sup> and inorganic materials.<sup>[21,26]</sup> Among these, inorganic materials are particularly appealing for good longevity and performance of the devices, being less volatile and lighter than organic polymers.<sup>[27]</sup> For example, the potential of a cesium iodide (CsI) interlayer for enhancing solar cell performance, particularly in LHP-based systems, has been highlighted by Wang et al. who employed vacuum evaporation to deposit the CsI layer on top and bottom of the MAPbI<sub>3</sub> perovskite layer. This led to a dramatic improvement in the film morphology, in turn boosting the device's performance and stability.<sup>[28]</sup> CsI interlayer has also been successfully employed in tin halide perovskite solar cells. Its addition enabled a decrease in the series resistance, and an enhancement in the shunt resistance, which in turn helped in improving the fill factor of the devices.<sup>[29]</sup> Baumeler et al. recently studied the impact of different metal iodide passivation layers on LHP, revealing that CsI significantly improves both solar cell performance and operational stability.<sup>[30]</sup>

To the best of our knowledge inorganic interlayers, such as CsI, have never been considered for interface engineering in PIMs based solar cell applications. Inspired by similar work on LHP- and tin-based solar cells,<sup>[28–30]</sup> here we introduce a CsI interlayer at the interface between the ABI active layer and the HTL in the solar cell stack to address some of the key shortcomings of ABI solar cells, i.e., the inefficient charge extraction as well as ion migration and diffusion. We thermally evaporated CsI thin film on top the ABI film and conducted a thorough comparative analysis with respect to a control device. We employed optical spectroscopy, electron microscopy, and electrical measurements to establish the superiority and highlight the importance of interface engineering in ABI and similar PIMs.

Our observations reveal the enhancement in device performances, attributing it to improved ABI|HTL interface, better charge extraction, and reduced hysteresis.

## 2. Results and Discussion

ABI thin films are deposited by spin-coating a BiI<sub>3</sub>:AgI precursor solution, followed by a modified two-step thermal annealing (see further details in Experimental Section, Supporting Information, SI). In contrast to the typical one-step annealing methods reported earlier,<sup>[16,17]</sup> we find that a two-step annealing process enhances the film coverage of ABI. The films subjected to a single-step annealing process exhibit incomplete surface coverage, as confirmed by scanning electron microscopy (SEM) topography images (Figure S1, Supporting Information). However, the morphology of ABI film is still suboptimal, with evident gaps between the crystalline domains (see a high-resolution SEM top-view image in Figure 1a), which leads to poor charge transfer at the ABI|HTL interface. We deposit a 10 nm CsI passivation layer atop the ABI film by vacuum thermal evaporation. The CsI thickness of 10 nm is selected based on the PCE optimization of the corresponding solar cells (see Figure S2, Supporting Information). The schematic representation of the film deposition procedure, which includes the spin coating of ABI, two-step annealing, and subsequent evaporation of CsI interlayer atop ABI film, is depicted in Figure 1a. It is evident that the addition of CsI layer fills the gaps of ABI film (Figure 1a), leading to effective physical interaction between the ABI and the HTL. The significance of these morphological changes lies in the potential impact on the performance and reliability of devices employing ABI|CsI.

The X-Ray diffraction (XRD) analysis of the as-deposited ABI film confirms the formation of ABI (01-075-5443), as shown in Figure 1b. A highly crystalline phase of ABI is obtained with R3m symmetry. The prominent diffraction peaks at 12.8°, 24.1°, 25.2°, 29.4°, 41.6°, and 51.8° correspond to the (003), (010), (102), (104), (110), and (204) reflections, respectively.<sup>[31]</sup> As expected, small amounts of AgI impurity phases are also detected, due to the Ag-rich precursor composition used to synthesize ABI.<sup>[32,33]</sup> Upon the deposition of CsI atop ABI film, the XRD analysis confirms that, as expected, ABI's structure remains unaltered, indicating that CsI is an independent interfacial layer, whose growth does not alter the structural properties of ABI. This is because the CsI layer is exceptionally thin (10 nm). On the contrary, the presence of CsI is confirmed by the presence of a characteristic peak of CsI at 27° corresponding to the (110) reflections (see the inset of Figure 1b, which shows a magnified view of the XRD patterns). With the help of energy dispersive X-ray spectroscopy (EDS), it is possible to identify the elemental composition of ABI and ABI|CsI films (see Figure S3, Supporting Information). The EDS mapping shows a uniform elemental distribution in both samples, with a calculated composition for the ABI thin film of Ag<sub>3</sub>Bi<sub>0.95</sub>I<sub>5.87</sub>. The slight deviation from nominal bismuth and iodine values is attributed to the Ag-I reach phase identified in the XRD analysis.

A comparative UV-visible spectroscopy study on ABI films before and after the deposition of CsI interlayer verifies that no changes in the optical properties are noted, see Figure 1c. As expected, similar absorption properties are achieved in both

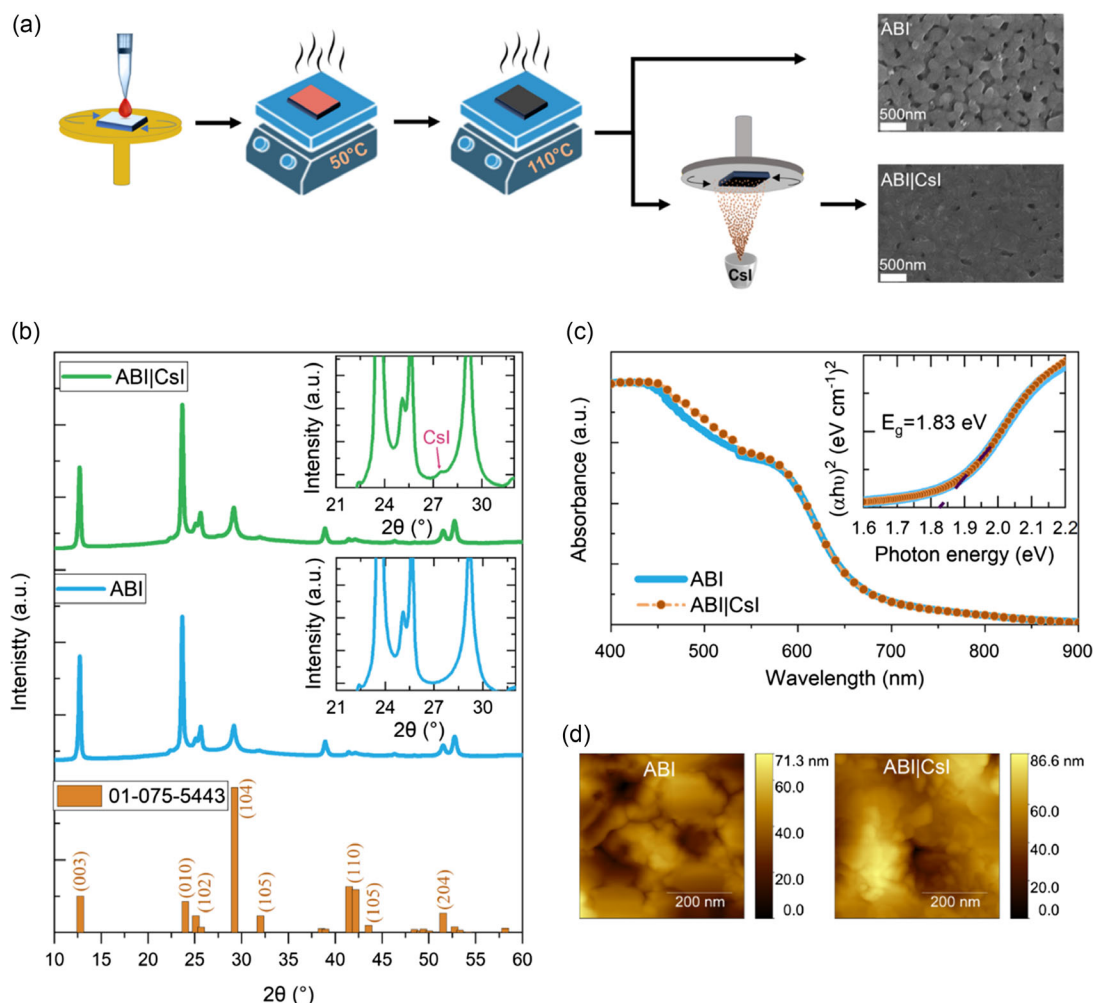


**Figure 1.** a) Summary of ABI film deposition process without and with CsI evaporated film atop. b) XRD patterns of ABI and ABI|CsI films deposited on glass substrates along with the reference pattern of ABI (01-075-5443), c) absorption spectra of ABI and ABI|CsI films deposited on glass substrates. Tauc plots are also presented in the inset. d) AFM topography images for ABI and ABI|CsI films.

cases and the bandgap (1.83 eV, estimated from Tauc plot shown in the inset in Figure 1c, and in agreement with previous reports<sup>[33]</sup>) remains unchanged, further supporting the suitability of CsI as an interlayer.

In order to further confirm the filling of pinholes enabled by the CsI interlayer suggested by the SEM analysis and their implication in the relative performance enhancement of the corresponding photovoltaics, we perform atomic force microscopy (AFM) and Kelvin probe force microscopy (KPFM) that relate the surface morphology and roughness to the electrical performance. AFM topographic images of ABI and ABI|CsI films are presented in Figure 1d. We found that surface roughness decreases after the CsI layer deposition on top of the ABI film, as demonstrated by the surface root-mean-square roughness (RMS) value decreasing from 42.48 to 20.08 nm. In addition, the ABI|CsI film exhibits fewer holes compared to the ABI film. These results confirm that depositing the CsI layer leads to filling of the gaps between grains and reduces pinholes in the film resulting in a smooth surface, conforming the observations from the analysis of the top-view SEM images (Figure 1a). These

findings indicate that surface smoothness and reduction in the defects at the ABI|HTL interface may lead to improvements in charge transfer and photovoltaic parameters of the corresponding solar cells. We then employed KPFM to measure the surface potential of the thin films. Surface potential mappings under switching the illumination on and off, and the corresponding plot of the KPFM surface potential as a function of time for ABI and ABI|CsI films, are presented in Figure S4, Supporting Information. Under illumination, the generation of electron–hole pairs occurs, resulting in negative surface potential. When illumination is switched off, the electrons and holes recombine, causing a positive surface potential. On the contrary, ABI film shows nonhomogeneous surface potential under both light and dark while the presence of a CsI layer on top of ABI reduces inhomogeneities in surface potential, further confirming the effectiveness of CsI interlayer in mitigating the poor morphology in ABI thin films.

Our Raman spectroscopy study for ABI and ABI|CsI films helps to understand the vibrational modes, which may suggest possible changes in the structural properties of the material.

To the best of our knowledge, the Raman spectra for ABI have never been reported before. We show that ABI thin film is Raman active, and the Raman spectra are presented in **Figure 2a** for both ABI and ABI|CsI thin films. The spectra comprise distinct peaks in the low wavenumber range of 50–150  $\text{cm}^{-1}$ , attributed to lattice vibrations. Specifically, two notable peaks at 112 and 130  $\text{cm}^{-1}$  are identified as Bi-I stretching modes,<sup>[34]</sup> while the peak with low intensity at 84  $\text{cm}^{-1}$  corresponds to the  $E_g$  stretching mode of Bi-I.<sup>[35]</sup> A set of overlapping peaks below 75  $\text{cm}^{-1}$  with a low-intensity profile can be identified for various bending modes and Bi-I-Bi interactions.<sup>[36]</sup> Although no shift in the Raman spectrum is observed, a decrease in Raman intensity is noted after depositing the CsI layer, which could be caused by a longer photon penetration length in the material.

The unchanged properties observed in XRD, absorption properties (including optical band gap), and Raman spectra evidence that the presence of the CsI interlayer does not alter the fundamental characteristics of ABI. This suggests that the  $\text{Cs}^+$  does not diffuse into the ABI grains during the vacuum thermal evaporation; instead, it fills gaps in the ABI film and remains on the surface.<sup>[30]</sup> X-ray photoelectron spectroscopy (XPS), being a surface characterization technique, can thus provide essential information on such a thin (10 nm) CsI interlayer. **Figure 2b** shows

the XPS survey plot for ABI film before and after the deposition of CsI interlayer. High-resolution XPS spectra of Ag 3d, I 3d, Bi 4f, and Cs 3d are as plotted in **Figure 2c–f**, respectively. The spectra show representative Ag 3d peaks of ABI located at 368.2 eV attributed to 3d 5/2 and 374.3 eV attributed to 3d 3/2 energies states.<sup>[14,16]</sup> In the case of the ABI|CsI, additional peaks corresponding to Cs 3d (3d 3/2 and 3d 5/2) energy states clearly appear, as expected, indicating the formation of CsI interlayer. The high-resolution XPS results indicate significant shifts toward higher binding energy in the peaks of Ag 3d, I 3d, and Bi 4f after the deposition of the CsI interlayer. Specifically, the Ag 3d peaks shifted by 0.7 eV, while the I 3d and Bi 4f peaks shifted to higher binding energies by 0.5 eV. These shifts suggest a strong interaction between the CsI interlayer and the ABI film.<sup>[37]</sup> The absence of oxygen in the XPS survey plot rules out the possibility of oxides formation, which helps us further assert that a strong molecular interaction exists at the ABI|CsI interface.

To validate our hypothesis regarding the role of the CsI interlayer in enhancing the efficiency of the ABI photovoltaic devices, solar cells are fabricated in an *n-i-p* mesoscopic architecture with “FTO/*c*-TiO<sub>2</sub>/*m*-TiO<sub>2</sub>/(ABI or ABI|CsI)/Spiro-OMeTAD/Au” configuration, wherein *c*-TiO<sub>2</sub> and *m*-TiO<sub>2</sub> are the compact and the mesoporous titanium dioxide electron transport layer

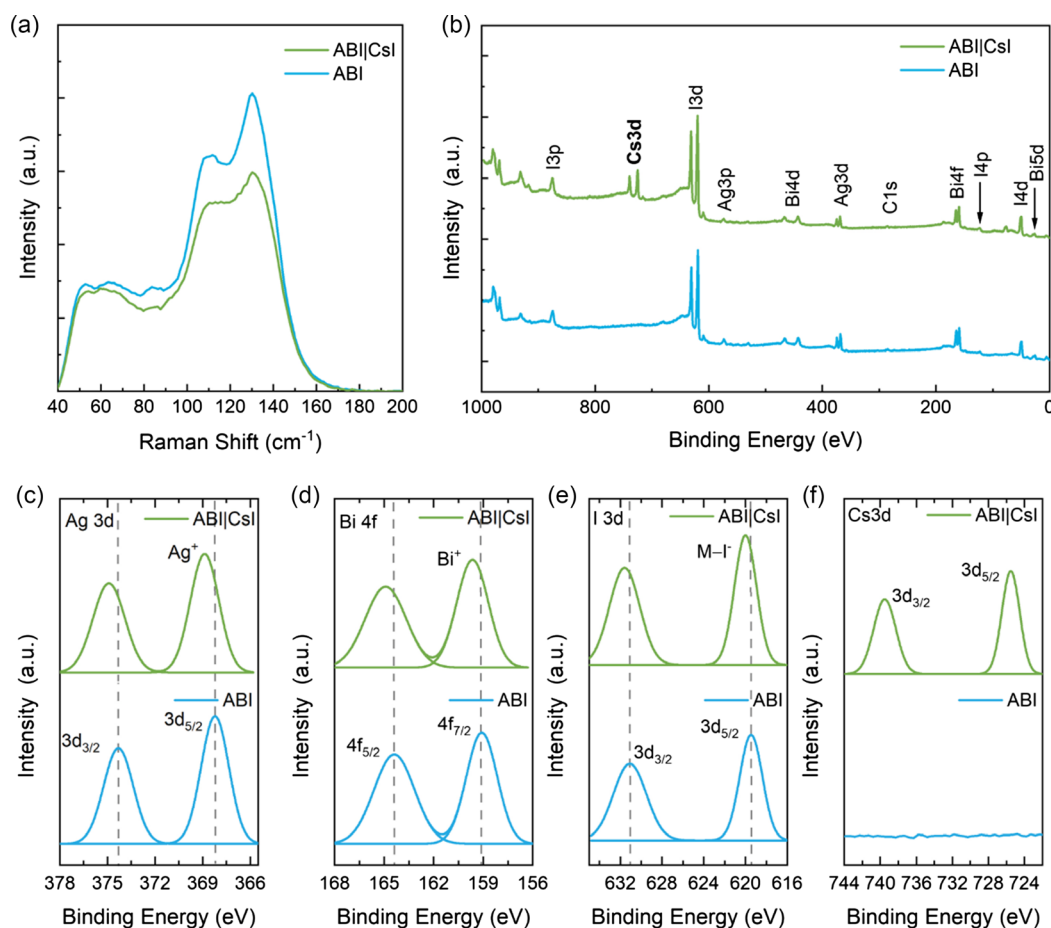


**Figure 2.** a) Raman spectra of the ABI and ABI|CsI films. b) XPS S survey spectra of the ABI and ABI|CsI films. High-resolution XPS spectra of c) Ag 3d, d) Bi 4f, e) I 3d, and f) Cs 3d for the ABI and ABI|CsI films.

(ETL), and Spiro-OMeTAD (2,2',7,7'-Tetrakis[N,N-di(4-methoxyphenyl)amino]-9,9'-spirofluorene) is HTL. The scheme of a typical device stack containing ABI|CsI is depicted in **Figure 3a**.

First, we aim at understanding whether the annealing of CsI interlayer has any influence on the performance of ABI|CsI photovoltaics. According to a recent report, the annealing of CsI interlayer at 140 °C leads to intercalation with the absorber layer, contributing to an enhancement in the performance of lead-based perovskite solar cells.<sup>[28]</sup> Hence, we examine three annealing temperatures for CsI atop ABI: room temperature (RT), 100 °C, and 150 °C. **Figure S5**, Supporting Information, shows the statistical distribution of PCE values of the ABI solar cells with CsI interlayer at different annealing temperatures. In contrast to the previous report,<sup>[28]</sup> in our case, the best photovoltaic performance is achieved with a CsI interlayer annealed at room temperature, while their PCE progressively decreases as the annealing temperature is increased.

After ensuring the optimization of the CsI deposition, we evaluate the effect of CsI on the performance of ABI solar cells. **Figure 3b** shows a comparison between the current density ( $J$ )-voltage ( $V$ ) curves of the champion ABI and ABI|CsI devices

under 1-Sun illumination (AM 1.5 G, 100 mW cm<sup>-2</sup>). The statistical distribution of the photovoltaic parameters is presented in **Figure 3c** for ABI and ABI|CsI devices, while the average values of PCE, fill factor (FF), short-circuit current density ( $J_{sc}$ ), and open-circuit voltage ( $V_{oc}$ ) are reported in Table S1, together with their standard deviations. While the champion ABI device displays a PCE of 1.94% (average PCE = 1.85%) consistent with a previous report focusing on the same device structure,<sup>[14]</sup> the champion ABI|CsI device demonstrates a notably higher PCE of 2.27% (average PCE = 2.15%), showing an increase of almost 20% compared to the control ABI device. This marks a notable advancement when compared to previously reported ABI-based devices and it represents, to the best of our knowledge, the highest reported PCE of ABI cells employing a similar device architecture and Spiro-OMeTAD as the HTL. Overall, the increase in FF of ABI|CsI-based devices (average FF = 63.7%) compared to ABI-based counterparts (average FF = 58.1%) is the major contributor to a general PCE enhancement. In addition, a slight increase in  $J_{sc}$  from 4.95 ± 0.12 to 5.30 ± 0.15 mA cm<sup>-2</sup> is also observed in cells adopting the CsI interlayer. The FF and  $J_{sc}$  increase could be attributed to the enhanced coverage of the

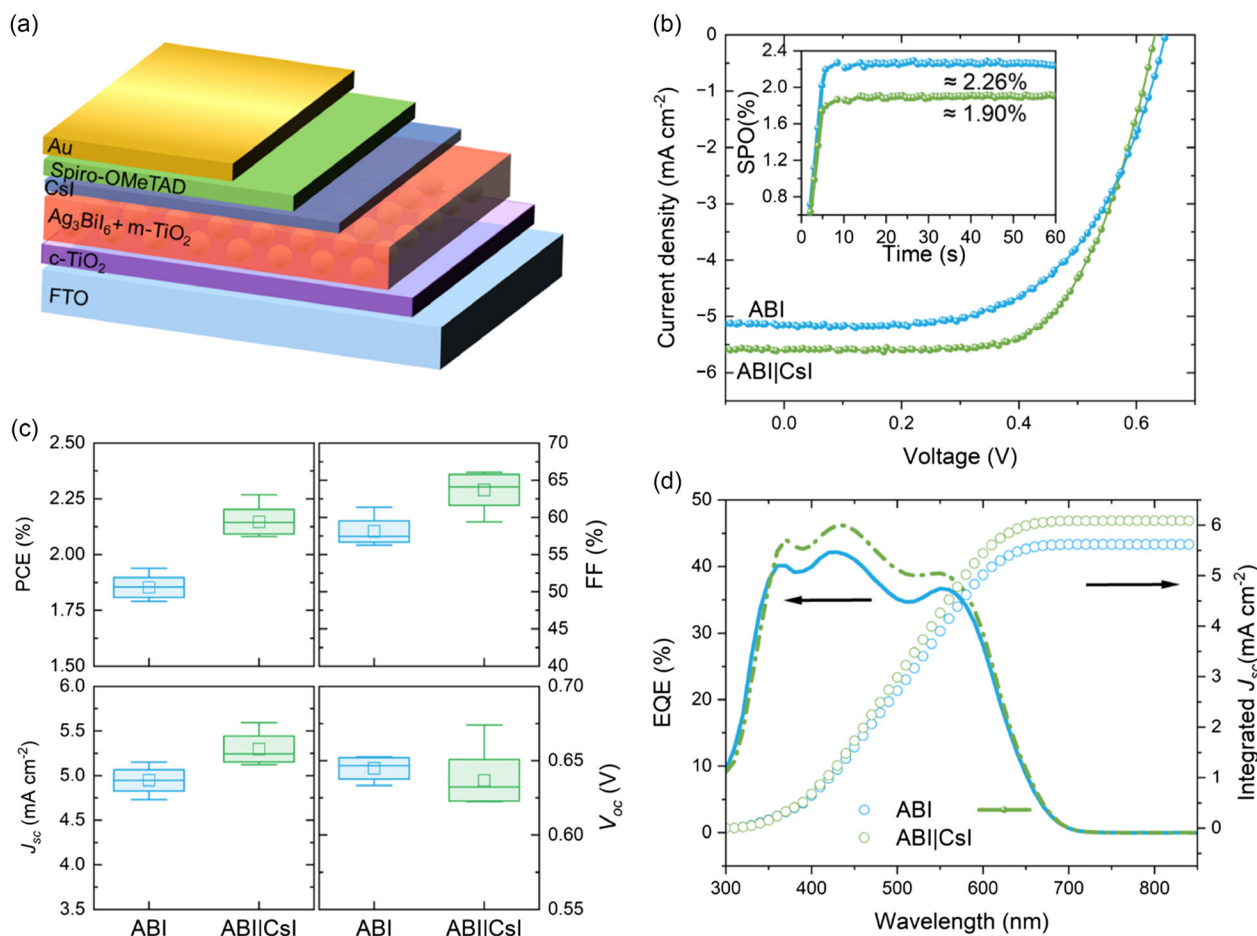


**Figure 3.** a) Scheme of a typical device stack of ABI|CsI solar cells. b)  $J$ - $V$  curves of the champion devices of ABI and ABI|CsI-based solar cells. The inset shows the stabilized power output at the maximum power point. c) Statistical distribution (over 15 devices) of the photovoltaic parameters of ABI and ABI|CsI solar cell devices under 1-Sun illumination. d) EQE spectra and the integrated  $J_{sc}$  curves of the champion devices of ABI and ABI|CsI-based solar cells.

absorber film upon CsI thin film deposition, as will be demonstrated with the support of the microscopy studies presented at the end of this section.

To verify the reliability of the champion PCE values, stabilized power output (SPO) measurements at the maximum power point are performed (inset of Figure 3b). The SPO values of the ABI ( $\approx 1.90\%$ ) and ABI|CsI ( $\approx 2.26\%$ ) closely match their PCE values of ABI (1.94%) and ABI|CsI (2.27%), respectively. The negligible mismatch of SPO and PCE values for ABI|CsI indicates that hysteresis has a weak influence on the resulting SPO. The external quantum efficiency (EQE) spectra and integrated  $J_{sc}$  extracted from EQE of the champion devices are presented in Figure 3d. The integrated  $J_{sc}$  values are remarkably close to the  $J_{sc}$  obtained from the  $J-V$  curve, further confirming the accuracy of our experiments.

Figure S6, Supporting Information, shows the box chart of the hysteresis index for both ABI and ABI|CsI-based solar cells. It is noteworthy that the introduction of the CsI interlayer in ABI-based solar cells leads to a significantly reduced hysteresis. In perovskite photovoltaics, hysteresis in current-voltage characteristic curves has been linked to ion migration.<sup>[38]</sup> A reduction in the hysteresis in ABI|CsI cells may result from the role of CsI interlayer serving as a barrier to prevent undesirable ion migration and diffusion.

The semi-logarithmic dark  $J-V$  curves are presented in **Figure 4a**. A striking feature is that the dark current for the ABI|CsI-based solar cells is much lower than that of the ABI devices, suggesting a decreased leakage current. This suggests that the addition of CsI interfacial layer helps to suppress the interfacial defects, which impact the FF of the solar cells.<sup>[39,40]</sup>

To investigate the charge carrier dynamics, the  $V_{oc}$  decay measurement is carried out. The comparative  $V_{oc}$  decay plot for ABI- and ABI|CsI-based devices is shown in Figure 4b. When illuminated, the solar cells undergo polarization, which affects the behavior of the  $V_{oc}$  decay curve. The device's overall photovoltage is influenced by the Fermi level splitting in the system, which is caused by the polarized voltage.<sup>[41]</sup> The first component with a very fast voltage drop is caused by the polarized voltage in the absorber layer disappearing very quickly as it relaxes from a polarized state to neutral. For both ABI- and ABI|CsI-based devices this rapid decline is equivalent. The slow decay, or second component, is caused by the slow back transfer of electrons from  $TiO_2$  to the perovskite layer or HTL. This process leads to additional potential loss to 0 V and approaches the dark equilibrium. In the case of ABI|CsI-based devices, this decay is comparatively slow. The carrier lifetimes ( $T_n$ ) can be derived from  $V_{oc}$  decay curve using the following equation<sup>[42]</sup>

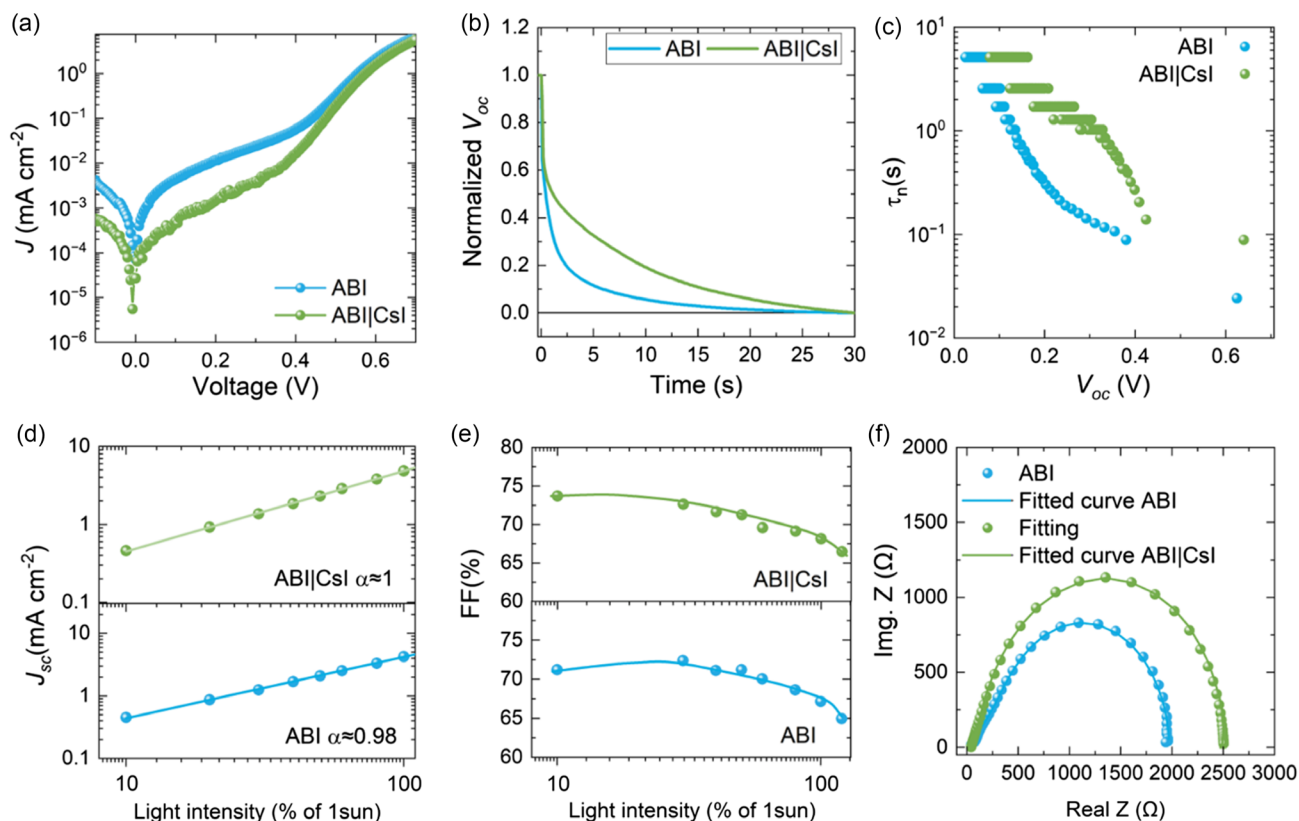


**Figure 4.** a) Semi-logarithmic dark  $J-V$  curves, b) Open-circuit voltage decay, c) Carrier lifetime extracted from open-circuit voltage decay as a function of  $V_{oc}$ . d) Log-log trends of  $J_{sc}$  of the ABI|CsI and ABI devices versus light intensity respectively. e) Fill factor trend of the ABI|CsI and ABI devices versus light intensity. f) Nyquist plots recorded at 0.5 V with symbols and lines showing experimental data and the corresponding fits based on the equivalent circuit model, respectively.

$$\tau_n = -\frac{k_B T}{e} \left( \frac{dV_{oc}}{dt} \right)^{-1} \quad (1)$$

where  $k_B$  is the Boltzmann constant,  $T$  is the temperature (K),  $e$  is the elementary charge, and  $t$  is the time after switching off the illumination source. The ABI|CsI-based solar cell shows high carrier lifetime values (Figure 4c) within the  $V_{oc}$  range in comparison with those of ABI device. The longer carrier lifetime values, along with slow  $V_{oc}$  decay, for ABI|CsI-based devices suggest that the recombination rates are lower than that for ABI-based devices. This explains the higher  $J_{sc}$  and FF values in solar cells (Figure 3c).

Light intensity-dependent characteristics, performed in the light intensities range of 0.1–1.2 Sun, provide deeper insights into the effect of CsI interlayer on the performance of devices. Figure 4d shows the variation of  $J_{sc}$  as a function of light intensity for ABI|CsI and ABI solar cells, respectively. The slope of a log-log plot of the variation of  $J_{sc}$  as a function of light intensity typically represents the exponent ( $\alpha$ ) factor in the power-law relationship between the current density and light intensity ( $J \propto I^\alpha$ ). The  $\alpha$  values extracted from Figure 4d for ABI|CsI ( $\alpha \approx 1$ ) and ABI ( $\alpha \approx 0.98$ ) solar cells indicate the absence of significant space-charge effects in the devices.<sup>[43]</sup> On the contrary, a slight increase in  $\alpha$  value for ABI|CsI ( $\alpha \approx 1$ ) suggests charge collection efficiency improvement that contributes to an enhancement in  $J_{sc}$  compared to the ABI device. In general, the FF tends to increase as light intensity decreases for both devices owing to the negligible influence of series resistance, particularly at low light intensities (Figure 4e).<sup>[44,45]</sup> However, ABI|CsI devices demonstrate higher FF values at both low and high light intensities compared to the ABI counterparts. This difference may be attributed to the low series resistance in the case of ABI|CsI cells, as will be discussed later.

In order to investigate the charge recombination in both devices further, we carry out impedance spectroscopy (IS) experiments. The corresponding experimental results, together with the fitting curves, are shown in Figure 4f. The two observed arcs are simulated with independent parallel  $R_C$  components, while  $R_s$  is the series resistance of the charge collecting electrodes. The low frequency semicircle at the  $\text{TiO}_2$ |perovskite interface represents charge recombination in parallel with chemical capacitance, whereas the high frequency arc represents the counter electrode charge transport resistance in the perovskite|HTL.<sup>[46,47]</sup> The equivalent circuit and impedance parameters obtained by data fitting with the equivalent circuit are shown in Figure S7 and Table S2, Supporting Information, where  $R_{ct}$  and  $C_{ct}$  stand for the transport resistance and capacitance at the interface, respectively, and  $R_{rec}$  and  $C_{rec}$  indicate the recombination resistance and capacitance.<sup>[48,49]</sup> A series resistance ( $R_s$ ) of 6.16 and 4.84  $\Omega \text{ cm}^2$  are obtained for ABI- and ABI|CsI-based devices, respectively. A low series resistance suggests better electron movement through the bulk of the device leading to high FF. The ABI|CsI and ABI devices have respective  $R_{ct}$  values of 27.03 and 43.12  $\Omega \text{ cm}^2$ , and  $R_{rec}$  values of 268.75 and 187.5  $\Omega \text{ cm}^2$ . ABI|CsI cell's lower  $R_{ct}$  indicates better charge transfer through the interface. Additionally, a high  $R_{rec}$  suggests less carrier recombination losses, which contributes to an improvement in the photocurrent and FF.

To investigate the air stability of the films, we kept them in air under 50% relative humidity and 25 °C for 222 days. Then we compared the XRD of aged films with freshly deposited films. The XRD results confirm that the ABI and ABI|CsI films possess superior stability (see Figure S8, Supporting Information). To verify the impact of the CsI interlayer on operational stability, we monitored the efficiency of the unencapsulated ABI and ABI|CsI-based solar cells at the maximum power point (MPP) under continuous 1 Sun illumination for 360 min (see Figure S9, Supporting Information). The ABI|CsI-based solar cell demonstrates better operational stability compared to the ABI-based solar cell. However, the efficiency of both ABI- and ABI|CsI-based solar cells rapidly decreased during the first 30 min, similar to other lead-free PIMs. Future research could focus on enhancing the operational stability of ABI solar cells under continuous 1 Sun illumination and explore the effects of the AgI impurity.<sup>[50,51]</sup>

### 3. Conclusions

In conclusion, the introduction of a thermally evaporated CsI interlayer has proven to be a pivotal strategy for enhancing the performance of solar cells based on  $\text{Ag}_3\text{BiI}_6$  (ABI). The champion ABI|CsI device demonstrates a noteworthy PCE of 2.27%, which is the highest ever reported for devices employing ABI absorber and Spiro-OMeTAD HTL. The CsI incorporation in the device structure, between ABI and the HTL, leads to a relative improvement of about 20% in the PCE with respect to the control ABI solar cell (PCE = 1.94%). The PCE increase in ABI|CsI-based devices is primarily attributed to a substantial increase in the short-circuit current density and fill factor, as a result of the improved interfacial interaction between ABI and HTL that leads to more effective charge transfer and reduced charge carrier recombination. The deposition method that we have adopted for CsI layer, i.e., thermal evaporation, is recommended over the conventional spin coating, as the underlying absorber layer remains unaltered. Our research not only contributes to the advancement of silver iodobismuthates research, among the most efficient perovskite-inspired materials for photovoltaics, but also underscores the importance of interface engineering in PIM-based solar cells, specifically highlighting the positive influence of CsI as an interlayer material in enhancing the overall performance of solution-processed ABI solar cells. This promising development opens up possibilities for further exploration and optimization of interface layers for improved solar cell efficiency and performance.

### Supporting Information

Supporting Information is available from the Wiley Online Library or from the author.

### Acknowledgements

B.A.-A. thanks Vilho, Yrjö and Kalle Väisälä Fund of the Finnish Academy of Science and Letters for the financial support. P.V. thanks Research Council of Finland (Decision No. 347772) and Jane & Aatos Erkko foundation (project: SOL-TECH) for the financial support. This work is part of the

Research Council of Finland Flagship Programme, Photonics Research and Innovation (PREIN), Decision No. 320165.

## Conflict of Interest

The authors declare no conflict of interest.

## Author Contributions

B.A.-A.: Conceptualization (lead); Data curation (lead); Formal analysis (lead); Funding acquisition (supporting); Investigation (lead); Methodology (equal); Validation (equal); Visualization (lead); Writing—original draft (lead); Writing—review and editing (equal). V.S.: Conceptualization (equal); Data curation (equal); Formal analysis (supporting); Investigation (supporting); Methodology (equal); Supervision (supporting); Validation (equal); Visualization (supporting); Writing—original draft (supporting); Writing—review and editing (equal). J.K.G.K.: Data curation (equal); Formal analysis (equal); Funding acquisition (supporting); Investigation (equal); Methodology (equal); Validation (equal); Visualization (equal); Writing—original draft (supporting); Writing—review and editing (supporting). A.T.: Data curation (equal); Formal analysis (equal); Investigation (equal); Methodology (equal); Validation (equal); Visualization (equal); Writing—original draft (supporting); Writing—review and editing (Supporting). R.N.: Data curation (equal); Formal analysis (equal); Investigation (equal); Methodology (equal); Validation (supporting); Visualization (supporting); Writing—review and editing (supporting). P.M.: Data curation (supporting); Formal analysis (supporting); Investigation (equal); Methodology (supporting); Visualization (supporting); Writing—review and editing (supporting). D.M.: Data curation (equal); Formal analysis (equal); Investigation (equal); Methodology (supporting); Validation (supporting); Visualization (supporting); Writing—review and editing (supporting). M.M.: Data curation (supporting); Funding acquisition (equal); Methodology (supporting); Supervision (supporting); Validation (supporting); Writing—review and editing (supporting). P.V.: Data curation (equal); Formal analysis (supporting); Funding acquisition (lead); Methodology (equal); Project administration (lead); Resources (lead); Supervision (lead); Validation (equal); Writing—original draft (supporting); Writing—review and editing (lead).

## Data Availability Statement

The data that support the findings of this study are available from the corresponding author upon reasonable request.

## Keywords

charge-transfer, CsI, perovskite-inspired materials, silver iodobismuthates, solar cells

Received: April 18, 2024  
Revised: June 29, 2024  
Published online:

- [1] NREL, *Best Research-Cell Efficiency Chart*, *Photovoltaic Research*, <https://www.nrel.gov/pv/cell-efficiency.html>.
- [2] J. Park, J. Kim, H. S. Yun, M. J. Paik, E. Noh, H. J. Mun, M. G. Kim, T. J. Shin, S. Il Seok, *Nature* **2023**, 616, 724.
- [3] J. Cao, F. Yan, *Energy Environ. Sci.* **2021**, 14, 1286.
- [4] W. Ke, C. C. Stoumpos, M. G. Kanatzidis, *Adv. Mater.* **2019**, 31, 1803230.

- [5] A. Babayigit, A. Ethirajan, M. Muller, B. Conings, *Nat. Mater.* **2016**, 15, 247.
- [6] J. Li, H. L. Cao, W. Bin Jiao, Q. Wang, M. Wei, I. Cantone, J. Lü, A. Abate, *Nat. Commun.* **2020**, 11, 310.
- [7] Y. T. Huang, S. R. Kavanagh, D. O. Scanlon, A. Walsh, R. L. Z. Hoye, *Nanotechnology* **2021**, 32, 379501.
- [8] A. Chakraborty, N. Pai, J. Zhao, B. R. Tuttle, A. N. Simonov, V. Pecunia, A. Chakraborty, J. Zhao, N. Pai, B. R. Tuttle, A. N. Simonov, V. Pecunia, *Adv. Funct. Mater.* **2022**, 32, 2203300.
- [9] I. Turkevych, S. Kazaoui, E. Ito, T. Urano, K. Yamada, H. Tomiyasu, H. Yamagishi, M. Kondo, S. Aramaki, *ChemSusChem* **2017**, 10, 3754.
- [10] G. K. Grandhi, D. Hardy, M. Krishnaiah, B. Vargas, B. Al-Anesi, M. P. Suryawanshi, D. Solis-Ibarra, F. Gao, R. L. Z. Hoye, P. Vivo, *Adv. Funct. Mater.* **2023**, 2307441.
- [11] N. B. Correa Guerrero, Z. Guo, N. Shibayama, A. K. Jena, T. Miyasaka, *ACS Appl. Energy Mater.* **2023**, 6, 10274.
- [12] M. Khazaei, K. Sardashti, C. C. Chung, J. P. Sun, H. Zhou, E. Bergmann, W. A. Dunlap-Shohl, Q. Han, I. G. Hill, J. L. Jones, D. C. Lupascu, D. B. Mitzi, *J. Mater. Chem. A* **2019**, 7, 2095.
- [13] K. W. Jung, M. R. Sohn, H. M. Lee, I. S. Yang, S. Do Sung, J. Kim, E. Wei-Guang Diao, W. I. Lee, *Sustain. Energy Fuels* **2017**, 2, 294.
- [14] N. Pai, J. Lu, T. R. Gengenbach, A. Seeber, A. S. R. Chesman, L. Jiang, D. C. Senevirathna, P. C. Andrews, U. Bach, Y. B. Cheng, A. N. Simonov, *Adv. Energy Mater.* **2019**, 9, 1803396.
- [15] Z. Zhang, Q. Sun, Y. Lu, F. Lu, X. Mu, S. H. Wei, M. Sui, *Nat. Commun.* **2022**, 13, 1.
- [16] A. Mutlu, C. Zafer, *Sol. Energy* **2022**, 234, 190.
- [17] M. C. Wu, R. Y. Kuo, Y. H. Chang, S. H. Chen, C. M. Ho, W. F. Su, *Oxford Open Mater. Sci.* **2020**, 1, itab017.
- [18] Y. Seo, S. R. Ha, S. Yoon, S. M. Jeong, H. Choi, D. W. Kang, *J. Power Sources* **2020**, 453, 227903.
- [19] M. C. Wu, Q. H. Wang, K. C. Hsiao, S. H. Chen, C. M. Ho, M. H. Jao, Y. H. Chang, W. F. Su, *Chem. Eng. J. Adv.* **2022**, 10, 100275.
- [20] A. Kulkarni, F. Ünlü, N. Pant, J. Kaur, C. Bohr, A. K. Jena, S. Öz, M. Yanagida, Y. Shirai, M. Ikegami, K. Miyano, Y. Tachibana, S. Chakraborty, S. Mathur, T. Miyasaka, *Sol. RRL* **2021**, 5, 2100077.
- [21] F. S. Ghoreishi, V. Ahmadi, M. Alidaei, F. Arabpour Roghabadi, M. Samadpour, R. Poursalehi, E. M. J. Johansson, *Phys. Chem. Chem. Phys.* **2022**, 24, 1675.
- [22] N. Y. Nia, F. Matteocci, L. Cina, A. Di Carlo, *ChemSusChem* **2017**, 10, 3854.
- [23] F. S. Ghoreishi, V. Ahmadi, R. Poursalehi, M. Boschloo, M. B. Samadpour, G. Boschloo, E. M. J. Johansson, *J. Power Sources* **2020**, 473, 228492.
- [24] G. A. Nemnes, C. Besleaga, A. G. Tomulescu, A. Palici, L. Pintilie, A. Manolescu, I. Pintilie, *Sol. Energy* **2018**, 173, 976.
- [25] I. Mora-Seró, J. Bisquert, F. Fabregat-Santiago, G. Garcia-Belmonte, G. Zoppi, K. Durose, Y. Proskuryakov, I. Oja, A. Belaidi, T. Dittrich, R. Tena-Zaera, A. Katty, C. Lévy-Clément, V. Barrioz, S. J. C. Irvine, *Nano Lett.* **2006**, 6, 640.
- [26] K. T. Cho, G. Grancini, Y. Lee, E. Oveisi, J. Ryu, O. Almora, M. Tschumi, P. A. Schouwink, G. Seo, S. Heo, J. Park, J. Jang, S. Paek, G. Garcia-Belmonte, M. K. Nazeeruddin, *Energy Environ. Sci.* **2018**, 11, 952.
- [27] A. Dualeh, T. Moehl, N. Tétreault, J. Teuscher, P. Gao, M. K. Nazeeruddin, M. Grätzel, *ACS Nano* **2014**, 8, 362.
- [28] L. Le Wang, M. Shahiduzzaman, E. Y. Muslih, M. Nakano, M. Karakawa, K. Takahashi, K. Tomita, J. M. Nunzi, T. Taima, *Nano Energy* **2021**, 86, 106135.
- [29] L. He, J. Cheng, L. Zhao, X. Chen, X. Zou, C. Zhang, J. Li, *Molecules* **2023**, 28, 6414.
- [30] T. P. Baumeler, E. A. Alharbi, G. Kakavelakis, G. C. Fish, M. T. Aldosari, M. S. Albishi, L. Pfeifer, B. I. Carlsen, J. H. Yum,

- A. S. Alharbi, M. D. Mensi, J. Gao, F. T. Eickemeyer, K. Sivula, J. E. Moser, S. M. Zakeeruddin, M. Grätzel, *ACS Energy Lett.* **2023**, *8*, 2456.
- [31] T. Oldag, T. Aussieker, H. L. Keller, C. Preitschaft, A. Pfitzner, Z. *Anorg. Allg. Chem.* **2005**, *631*, 677.
- [32] Y. Yuan, N. Robertson, *Sustain. Energy Fuels* **2023**, *7*, 1067.
- [33] A. Crovetto, A. Hajjafarassar, O. Hansen, B. Seger, I. Chorkendorff, P. C. K. Vesborg, *Chem. Mater.* **2020**, *32*, 3385.
- [34] M. S. Lassoued, T. Wang, A. Faizan, Q. W. Li, W. P. Chen, Y. Z. Zheng, *J. Mater. Chem. C Mater.* **2022**, *10*, 12574.
- [35] Y. Yang, C. Wang, J. Hou, J. Dai, *Mater. Lett.* **2003**, *57*, 2185.
- [36] X. Li, B. Traoré, M. Kepenekian, L. Li, C. C. Stoumpos, P. Guo, J. Even, C. Katan, M. G. Kanatzidis, *Chem. Mater.* **2021**, *33*, 6206.
- [37] K. Zou, Q. Li, J. Fan, H. Tang, L. Chen, S. Tao, T. Xu, W. Huang, *ACS Mater. Lett.* **2022**, *4*, 1101.
- [38] H. Dixit, B. Boro, S. Ghosh, M. Paul, A. Kumar, T. Singh, *Phys. Status Solidi* **2022**, *219*, 2100823.
- [39] X. Gao, J. Li, S. Gollon, M. Qiu, D. Guan, X. Guo, J. Chen, C. Yuan, *Phys. Chem. Chem. Phys.* **2017**, *19*, 4956.
- [40] J. Liang, X. Han, J. H. Yang, B. Zhang, Q. Fang, J. Zhang, Q. Ai, M. M. Ogle, T. Terlier, A. A. Martí, J. Lou, *Adv. Mater.* **2019**, *31*, 1903448.
- [41] Q. Wang, *J. Phys. Chem. C* **2018**, *122*, 4822.
- [42] A. Zaban, M. Greenshtein, J. Bisquert, S. Berner, H. Suzuki, H. Yanagi, D. Schlottwein, S. Ivan, H. Guentherodt, T. A. Jung, J. V. Barth, J. Weckesser, C. Cai, O. Jeandupeux, K. Kern, A. De Vita, P. Rev Lett, P. Wu, Q. D. Zeng, S. D. Xu, C. Wang, S. X. Yin, C. L. Bai, H. B. Yu, C. S. Jiang, P. Ebert, X. D. Wang, J. M. White, Q. Niu, Z. Zhang, X. H. Qiu, B. Xu, H. N. Wang, C. J. Li, S. L. Xu, Y. H. Qiao, L. J. Wan, A. Zaban, M. Greenshtein, J. Bisquert, *ChemPhysChem* **2003**, *4*, 859.
- [43] V. Pecunia, Y. Yuan, J. Zhao, K. Xia, Y. Wang, S. Duhm, L. Portilla, F. Li, *Nanomicro Lett.* **2020**, *12*, 1.
- [44] Y. Galagan, E. W. C. Coenen, B. Zimmermann, L. H. Slooff, W. J. H. Verhees, S. C. Veenstra, J. M. Kroon, M. Jørgensen, F. C. Krebs, R. Andriessen, Y. Galagan, R. Andriessen, E. W. C. Coenen, B. Zimmermann, L. H. Slooff, W. J. H. Verhees, S. C. Veenstra, J. M. Kroon, M. Jørgensen, F. C. Krebs, *Adv. Energy Mater.* **2014**, *4*, 1300498.
- [45] M. Chegaar, A. Hamzaoui, A. Namoda, P. Petit, M. Aillerie, A. Herguth, *Energy Proc.* **2013**, *36*, 722.
- [46] M. Hu, L. Liu, A. Mei, Y. Yang, T. Liu, H. Han, *J. Mater. Chem. A Mater.* **2014**, *2*, 17115.
- [47] J. A. Christians, R. C. M. Fung, P. V. Kamat, *J. Am. Chem. Soc.* **2014**, *136*, 758.
- [48] J. Song, E. Zheng, X. F. Wang, W. Tian, T. Miyasaka, *Sol. Energy Mater. Sol. Cells* **2016**, *144*, 623.
- [49] D. Liu, J. Yang, T. L. Kelly, *J. Am. Chem. Soc.* **2014**, *136*, 17116.
- [50] B. Al-Anesi, G. Krishnamurthy Grandhi, A. Pecoraro, V. Sugathan, A. Belén Muñ Oz-García, M. Pavone, P. Vivo, *J. Phys. Chem. C* **2024**, *128*, 9446.
- [51] G. K. Grandhi, B. Al-Anesi, H. Pasanen, H. Ali-Löyty, K. Lahtonen, S. Granroth, N. Christian, A. Matuhina, M. Liu, A. Berdin, V. Pecunia, P. Vivo, *Small* **2022**, *18*, 2203768.